2 Hernandez-Nunez A, Dauden E, Moreno de Vega MJ *et al.* Widespread biphasic amyloidosis: response to acitretin. *Clin Exp Dermatol* 2001; **26**: 256–259.
3 Chang YT, Wong CK, Chow KC *et al.* Apoptosis in primary cutaneous amyloidosis. *Br J Dermatol* 1999; **140**: 210–215.
4 Behr FD, Levine N, Bangert J. Lichen amyloidosis associated with atopic dermatitis: clinical resolution with cyclosporine. *Arch Dermatol* 2001; **137**: 553–555.
5 Ozkaya-Bayazit E, Kavak A, Gungor H *et al.* Intermittent use of topical dimethyl sulfoxide in macular and papular amyloidosis. *Int J Dermatol* 1998; **37**: 949–954.
6 Castanedo-Cazares JP, Lepe V, Moncada B. Lichen amyloidosis improved by 0.1% topical tacrolimus. *Dermatology* 2002; **205**: 420–421.
7 Khoo BP, Tay YK, Goh CL. Calcipotriol ointment vs. betamethasone 17-valerate ointment in the treatment of lichen amyloidosis. *Int J Dermatol* 1999; **38**: 539–541.
8 Grimmer J, Weiss T, Weber L *et al.* Successful treatment of lichen amyloidosis with combined bath PUVA photochemotherapy and oral acitretin. *Clin Exp Dermatol* 2007; **32**: 39–42.
9 Gupta R, Gupta S. Dexamethasone cyclophosphamide pulse therapy in lichen amyloidosus: a case report. *J Dermatolog Treat* 2007; **18**: 249–251.
10 Yoshida A, Takahashi K, Tagami H *et al.* Lichen amyloidosis induced on the upper back by long-term friction with a nylon towel. *J Dermatol* 2009; **36**: 56–59.
11 Liu HT. Treatment of lichen amyloidosis (LA) and disseminated superficial porokeratosis (DSP) with frequency-doubled Q-switched Nd:YAG laser. *Dermatol Surg* 2000; **26**: 958–962.
12 Sawamura D, Sato-Matsumura KC, Shibaki A *et al.* A case of lichen amyloidosis treated with pulsed dye laser. *J Eur Acad Dermatol Venereol* 2005; **19**: 262–263.
13 Aoki M, Kawana S. Lichen amyloidosis of the auricular concha: successful treatment with electrodesiccation. *J Dermatol* 2009; **36**: 116–117.
14 Hallel-Halevy D, Finkelstein E, Grunwald MH *et al.* Lichen amyloidosus treated by hydrocolloid dressings. *J Eur Acad Dermatol Venereol* 2004; **18**: 691–692.
15 Mizutani H, Yoshida T, Nouchi N *et al.* Topical tocoretinate improved hypertrophic scar, skin sclerosis in systemic sclerosis and morphea. *J Dermatol* 1999; **26**: 11–17.
16 Maddison B, Namazi MR, Samuel LS *et al.* Unexpected diminished innervation of epidermis and dermoepidermal junction in lichen amyloidosus. *Br J Dermatol* 2008; **159**: 403–406.

J Mater Sci: Mater Med
DOI 10.1007/s10856-011-4469-2

Biomechanical evaluation of porous bioactive ceramics after implantation: micro CT-based three-dimensional finite element analysis

Li-Mei Ren · Takaaki Arahira · Mitsugu Todo · Hideki Yoshikawa · Akira Myoui

Received: 22 April 2011 / Accepted: 18 October 2011

Abstract Hydroxyapatite ceramics have been widely investigated for bone regeneration due to their high biocompatibility. However, few studies focus on their mechanical characteristics after implantation. In this study, the finite element (FE) method was used to evaluate the mechanical properties of a fully interconnected porous hydroxyapatite (IPHA) over time of implantation. Based on the micro-CT images obtained from the experiments dealing with IPHA implanted into rabbit femoral condyles, three-dimensional FE models of IPHA (1, 5, 12, 24, and 48 weeks after implantation) were developed. FE analysis indicated that the elastic modulus gradually increased from 1 week and reached the peak value at 24 weeks, and then it kept at high level until 48 weeks postoperatively. In addition, as a local biomechanical response, strain energy density became to distribute evenly over time after the implantation. Results confirmed that the mechanical properties of IPHA are strongly correlated to bone ingrowth. The efficiency of the proposed numerical approach was validated in combination with experimental studies, and the feasibility of applying this approach to study such implanted porous bioceramics was proved.

L.-M. Ren (✉) · T. Arahira · M. Todo
Research Institute for Applied Mechanics, Kyushu University, Kasuga-koen 6-1, Kasuga, Fukuoka 816-8580, Japan
e-mail: lmren@riam.kyushu-u.ac.jp; limeiren@gmail.com

H. Yoshikawa · A. Myoui
Department of Orthopaedics, Osaka University, 2-2 Yamadaoka, Suita 565-0871, Japan

Published online: 23 November 2011

1 Introduction

Biomaterials play an important role in regenerative medicine, which aims to regenerate and replace lost or damaged tissues by initiating the natural regeneration process. Among modern biomaterials, hydroxyapatite (HA) ceramics are considered to be very promising candidates as bone substitutes, due to their composition similarity to inorganic components of natural bone, as well as high biocompatibility and good osteoconduction [1–3]. The commercial HA ceramics are available as porous blocks and dense granules. Porous HA ceramics were expected to exhibit better osteoconduction in view of the fact that porous structure allows bone tissue ingrowth [4].

However, few reports indicated that the pores of implanted HA are totally filled with newly formed bone and several clinical studies showed that the interpores remained empty for years [1, 4, 5], probably because of the limited interconnection of the pores. It is realized that the dimension and morphology of pores are important factors for an excellent osteointegration, and the size of interpore connections might be even more crucial rather than the size of pores themselves because interpore connections less than 2–3 μm in diameter do not allow osteogenic cell migration or vascularization into the pores [1]. Moreover, Lu et al. [6] investigated the effect of interconnections structure of porous HA ceramics on bone ingrowth and reported that the diameter of interconnecting pores needed to be more than 20 μm for osteoblasts to enter porous ceramics. However, although greater pore size or interconnecting pore size leads to greater osteoconduction, the compressive strength of porous ceramics and clinical usefulness are reduced in conditions with larger pore sizes [7].

Therefore, particular attention has been paid to develop HA bioceramics with large pore and adequate interpore

connections as well as adequate compressive strength [8]. In recent years, a fully interconnected porous HA (IPHA) has been developed by use of a "foam-gel" technique [4], which can achieve both high interconnecting porous structure and enough compressive strength. This novel IPHA has a porosity of about 75%, with macropores of 100–200 μm that are fully interconnected by openings of about 40 μm in diameter. In addition, its initial compressive strength is reported as about 10 MPa [4, 9]. Considering its high porosity, such initial compressive strength is rather high and gives IPHA a great advantage as bone substitute. The superior property has led to great interest in the investigations of IPHA. Tamai et al. [1] reported that this IPHA exhibits excellent osteoconductivity and bone ingrowth in animals. In clinical application, Yoshikawa et al. [4] and Yoshida et al. [10] have applied this material for the treatment of patients suffering from benign bone tumor and bone fracture, and obtained favorable clinical results. The biological response and performance such as bone tissue formation in IPHA is often evaluated by performing histomorphometrical analyses of histological sections, however few studies focus on its mechanical characteristics after implantation, which is closely associated with bone ingrowth. Although the use of compression test to evaluate the mechanical properties of bone materials is well documented, the preparation of samples remains time-consuming and labour-intensive. As an alternative, computer tomography (CT)-based finite element (FE) method is considered to have the advantage of accurate quantitative structural analysis.

Nowadays, micro CT-based FE modeling has demonstrated a significant contribution in the field of functional bone engineering [11]. One of the important advances is that different micro CT-based FE models have been established for the modeling of scaffold, in general, for the modeling of porous biomaterials. For instance, Lacroix et al. [12] evaluated the porous structures of two scaffolds and assessed the effect of structures on loading transfer. Sandino et al. [13] studied mechanical stimuli that influence cell proliferation and differentiation for bone tissue engineering. Furthermore, as a computational approach, FE method was applied by Byrne et al. [14] and Sturm et al. [15] to model the bone tissue regeneration within a standard-structured bone scaffold. Up to date, most FE investigations are contributed to the development of optimal scaffold design for tissue ingrowth. Despite these advances, however, few attempts have been devoted to assess the mechanical properties of porous bioceramics after implantation using FE method. In this study, the mechanical properties of the previously mentioned IPHA (NEOBONE®; Covalent Material, Tokyo, Japan) after implantation were evaluated by means of micro CT-based FE analysis. The micro-CT images were obtained from animal experiments with IPHA implanted into rabbit femoral condyles [9]. The time-dependent changes of the mechanical properties of IPHA were evaluated from an early time (1 week) to a long-term postoperative period of 1 year after the implantation.

2 Materials and methods

2.1 Structure characterization

The cross sections of NEOBONE® before implantation were observed by a field emission scanning electron microscope (SEM; S-4100, Hitachi, Japan). The structure was characterized regarding the pore arrangements, the interpore connections and the inner walls of the pores.

2.2 Microfocus computed tomography

The micro-CT images used in current study were obtained from experimental study, in which the NEOBONE® grafts were implanted into the femoral condyles of rabbits. The procedure of the animal experiments has been described in detail previously [9]. Here is a brief outline of the testing regime. A straight 2.5 cm skin incision was made over the medial femoral condyle and the fascia was split. Then a hole of 6 mm in diameter was drilled through the femoral condyle, after which a matching size cylindrical block (6 mm in diameter and 15 mm long) of NEOBONE® was implanted into the hole, and the fascia and skin were closed. At the end of the specified observation period, the rabbits were killed by intravenous administration of 5 ml of pentobarbital for mechanical and histological analyses. The animal experiments were conducted at the Animal Laboratory of the Faculty of Medicine at Osaka University, following the animal care guidelines. The formation of new bone in each implant was evaluated with a microfocus CT system (SMX-100CT-SV; Shimadzu, Kyoto, Japan). Each sample was scanned at 10 μm intervals at 50 kV and 200 μA.

2.3 Mechanical evaluation

Harvested bone tissues were frozen at −20°C after radiographic evaluation and were divided into three equal segments through the long axis of the cylindrical implant so that each implant was cut into 5 mm cylinders. Then $3 \times 3 \times 4$ mm^3 blocks were cut out from the center of each cylindrical specimen for compression testing at a speed of 1 mm/min with a servo-hydraulic materials testing machine (858 Mini Bionix II, MTS). The load–displacement curves were obtained and the compressive strength was examined.

2.4 FE method

In this study, MECHANICAL FINDER 6.0 software (Research Center of Computational Mechanics, Inc., Japan) was employed to construct models and perform calculations. Due to the computational time and memory capacity of FE analysis, smaller sections from each implant were modeled rather than the whole block. For each set of micro-CT images (1, 5, 12, 24, and 48 weeks after implantation), three different locations were chosen to build models. Consequently, in total 15 models were created. Figure 1 presents the extracted and meshed cubic models (500 μm on each edge) as an example which was indicated with red frames in Fig. 2. Typical models contain around 95,000 nodes and 500,000 tetrahedral elements. The average values of the simulation results in the three models were calculated to quantitatively evaluate and represent the results of the entire model. To determine the mechanical properties of NEOBONE®, a compressive loading condition was simulated as the top of each cubic model was fixed in all displacements whereas a uniform load of 1 N along vertical direction was applied on the bottom of the cube.

In the MECHANICAL FINDER software, the bone density of an element was determined from the average CT value (HU: Hounsfield Unit) of 17 points, which were composed of the center point and four points distributed on four lines connecting the center point to each apex of the tetrahedral element [16]. The bone density (ρ) of each FE was computed by the relationship as follows:

$$\rho = \begin{cases} 0.0 & (HU \leq 1) \\ (0.945 \times HU + 1.347) \times 10^{-3} & (HU > 1) \end{cases} \quad (1)$$

It should be pointed out that the above method is to calculate density of the natural bone, therefore an upper density limit of 3.16 g/cm^3 was adopted to make it suitable for the current case of artificial bone by reference to the theoretical density of HA [17, 18]. And Poisson's ratio was set as 0.4 [19]. The elastic modulus (E) of each FE can be determined based on the following equations proposed by Keyak et al. [19]:

$$E = \begin{cases} 0.001 & (\rho = 0.0) \\ 33900\rho^{2.20} & (0.0 < \rho \leq 0.27) \\ 5307\rho + 469 & (0.27 < \rho < 0.6) \\ 10200\rho^{2.01} & (\rho \geq 0.6) \end{cases} \quad (2)$$

The elastic modulus of each element was calculated by Eq. 2 and could be reflected in the FE models in terms of contours of elastic modulus distributions. In order to calculate an overall elastic modulus of each model, the

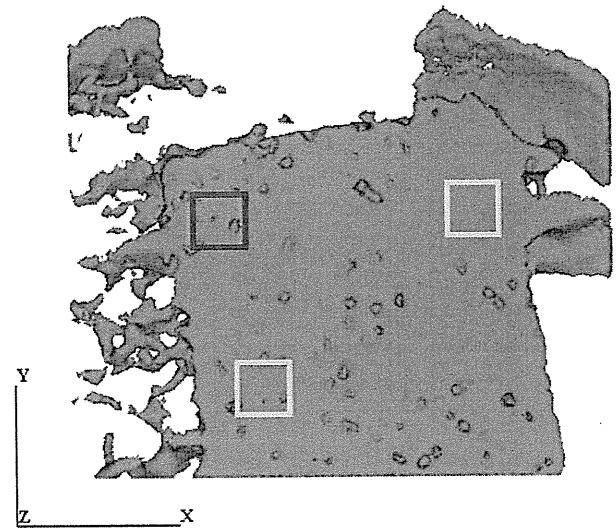

Fig. 2 Three locations indicated on micro-CT images to construct models

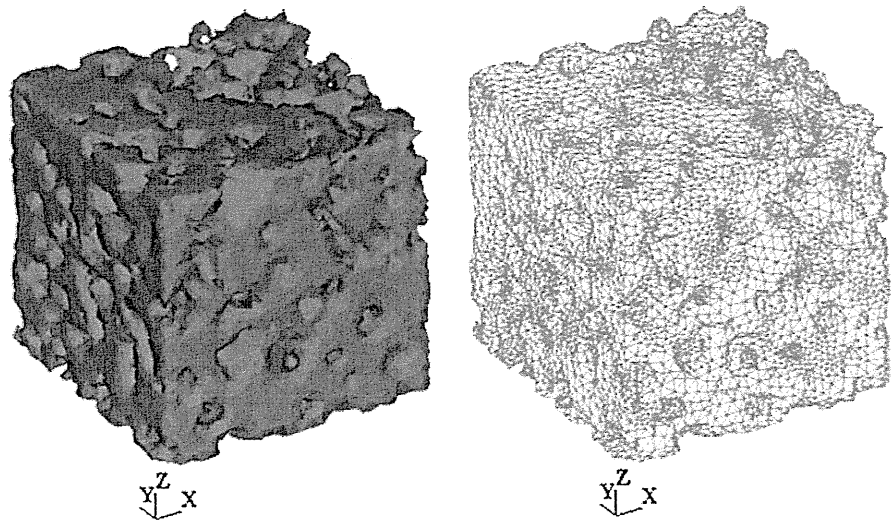

Fig. 1 The extracted and meshed three-dimensional models

calculated axial displacements of the loaded nodes are needed. The elastic modulus E (MPa) of each model was defined as:

$$E = (F/A)/(\Delta L/L_0) \tag{3}$$

where F (N) is the compressive load, A (mm^2) is the area of loaded surface, ΔL (mm) denotes the amount of deformation, and L_0 (mm) is the initial edge length of the cubic model. The amount of deformation ΔL was determined as the average axial displacements of all nodes on the loaded surface.

It is known that a fracture criterion of brittle ceramics under unidirectional compression can be expressed by the strain in the loading direction. It is therefore assumed that the compressive fracture of a NEOBONE® sample with bone tissue ingrowth can be controlled by the critical strain of NEOBONE® and the bone tissue filled within the porous structure does not affect the compressive fracture of the NEOBONE®-bone tissue composite system. In the current study, efforts were made to predict compressive strength by the calculated elastic modulus (e.g., from FE analysis). It is assumed that if the compressive strain of the representative model reaches the critical strain ε_c, and then fracture occurs. Under the critical strain criterion, the following equation can be derived to represent the correlation between strength and elastic modulus:

$$\sigma_c/\sigma_{c1W} = E/E_{1W} \tag{4}$$

where σ_c (MPa) and E (MPa) are the compressive strength and elastic modulus at any stage, respectively, and σ_{c1W} (MPa) and E_{1W} (MPa) denote the above parameters at 1 week after implantation.

Additionally, it should be pointed out that the pore size of the computational model tends to be smaller than the real pore size of NEOBONE® due to the resolution of CT images. As a result, the FE models have much lower porosities than the corresponding specimens. For instance, the initial material has a porosity of 75%, whereas the porosity of the FE model generated from the corresponding CT images is about 43% calculated by a two-dimensional approximation. It is generally assumed that the elastic modulus of a porous material is inversely proportional to the porosity. And a number of expressions for the relationship between elastic moduli and porosity have been proposed [20–23]. One of those frequently employed expressions takes the following form:

$$E = E_0(1 - \phi)/(1 + a\phi) \tag{5}$$

where E and E_0 represent the elastic modulus of porous materials and dense materials, respectively, ϕ denotes the volume fraction of porosity, and a (here $a = 1$) is a constant related to the Poisson's ratio of the dense material [20].

Due to the lower porosities of the models, the stiffness of the models becomes larger than the real one and therefore, the stress value (compressive strength) at the critical strain is overestimated. Then the modified compressive strength is given by:

$$\sigma_c' = \lambda\sigma_c = \frac{(1 - \phi_{true})(1 + \phi_{model})}{(1 + \phi_{true})(1 - \phi_{model})}\sigma_c \tag{6}$$

where σ_c' and σ_c denote the critical stress value (compressive strength) after and before modification; ϕ_{model} and ϕ_{true} are the porosity of numerical model and actual material, respectively. In Eq. 6, λ is a coefficient in relation to ϕ_{model} and ϕ_{true}.

3 Results

SEM observation demonstrated that most of the pores were similar in size and shape, as shown in Fig. 3a. The pores had several holes in their walls that connected to the adjacent ones. In addition, the pore walls are very smooth and formed by tightly bound HA particles (Fig. 3b).

The elastic modulus distribution of NEOBONE® at each stage (1, 5, 12, 24, and 48 weeks after implantation), as calculated by Eqs. 1 and 2, are presented in Fig. 4. A cut-view of each model is also displayed to show elastic modulus distribution on a section. There are no significant differences among the elastic modulus distribution contours. The maximum elastic modulus indicated in the all models is around 1,100–1,300 MPa, whereas the minimum varies in a range of 500–700 MPa.

To quantitatively assess the changes of overall stiffness, the elastic moduli of all models were determined by Eq. 3. The calculated results are as shown in Fig. 5, expressed by the average value and standard deviation. In Fig. 5 the measured elastic moduli of NEOBONE® from compression test are also presented. As an experimental method, the load–displacement curve from compression test can be converted into stress–strain curve by dividing the force by the cross-sectional area of the specimen and dividing the deformation by the original length of the specimen. The slope of the rising part of the curve is the elastic modulus. Both simulation and experimental data demonstrate that the elastic modulus increased from 1 to 24 weeks, and reached the peak value at 24 weeks. Afterwards, in the case of simulation, there is no significant decrease from 24 to 48 weeks after implantation. To get more insight into the effect of bone ingrowth on the changes of elastic modulus, a three-dimensional diagram displaying the correlation between bone mineral density (BMD) [9] and elastic modulus versus duration of implantation was presented in Fig. 6. The increase or decrease of BMD results in a similar change in the elastic modulus. In Fig. 6, the

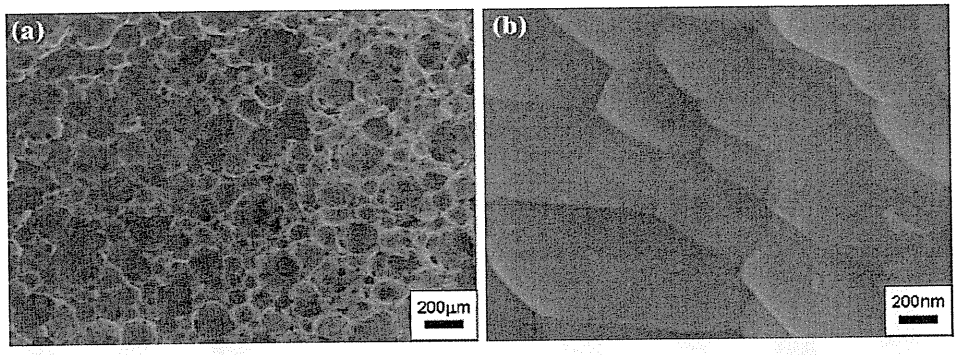

Fig. 3 SEM micrographs showing the cross-sectional morphology of IPHA (**a**) and the inner wall of pores (**b**)

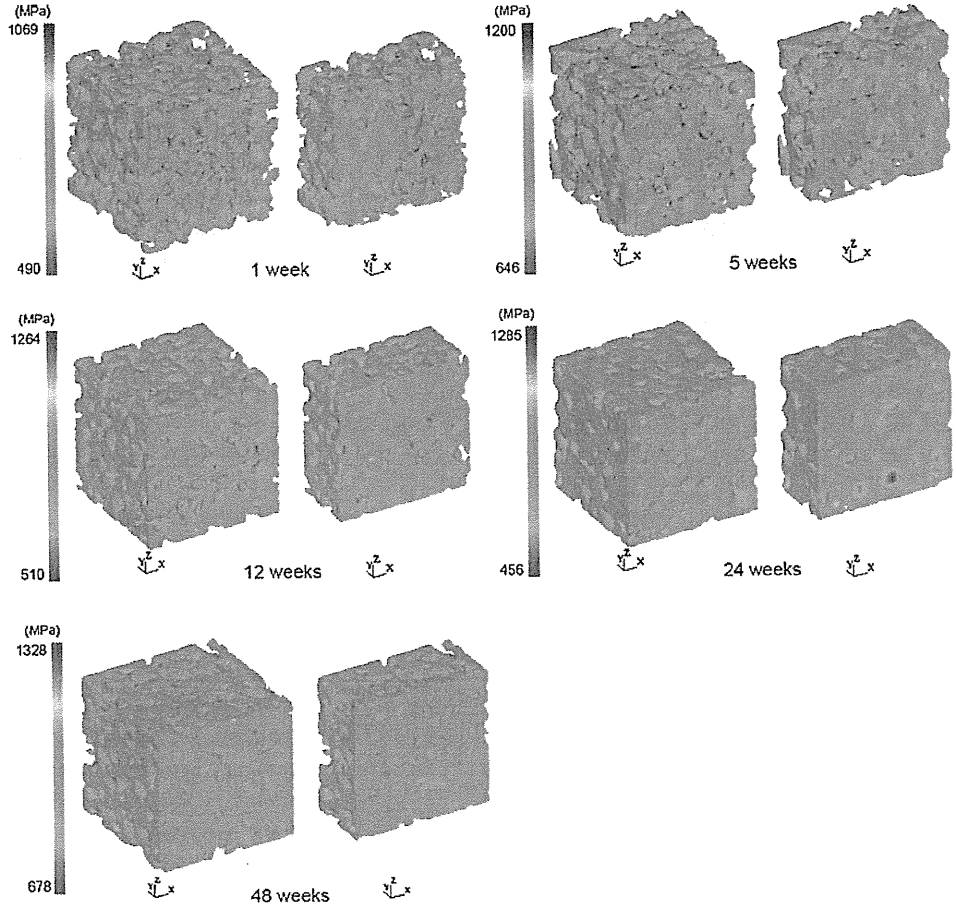

Fig. 4 Distribution of elastic modulus of NEOBONE® at 1, 5, 12, 24, and 48 weeks after implantation

slice-view from models of early postoperative period (1 week) and long-term period (48 weeks) after implantation were also included. The structural changes with the duration of surgery can be easily observed.

Variation of measured compressive strength and calculated elastic modulus is exhibited in Fig. 7. Naturally, the value magnitudes of them are different, but the curves display a similar tendency. Here, the calculated elastic modulus was used to predict compressive strength under the critical strain criterion. The FE predicted strength and the measured ones from compression test were normalized with their respective strength value at 1 week. Figure 8 shows the normalized compressive strength versus time of implantation. The simulation and experimental results demonstrate good agreements.

Figure 9 represents the strain energy density (SED) distribution in the models of NEOBONE® (1, 5, 12, 24, and 48 weeks after the implantation), and a cut-view of each

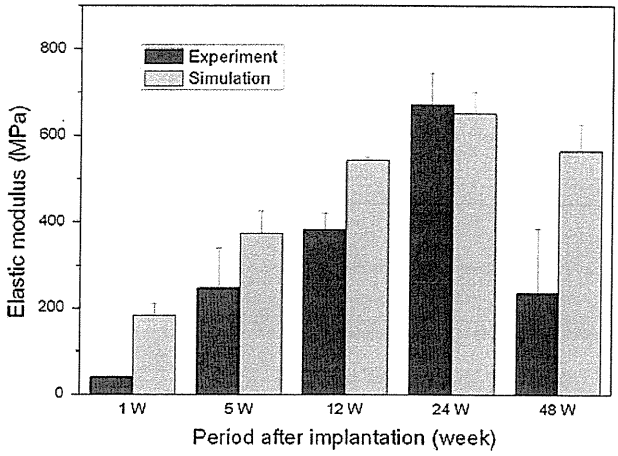

Fig. 5 Comparison of the elastic moduli obtained from the experiments and FE simulations

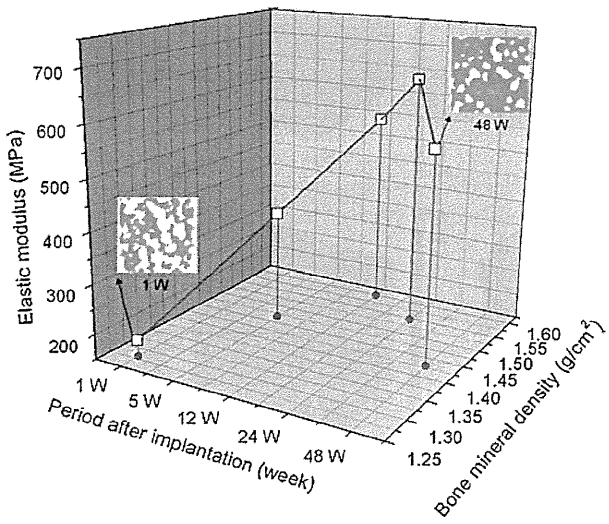

Fig. 6 The three-dimensional diagram displaying the correlation between BMD and elastic modulus

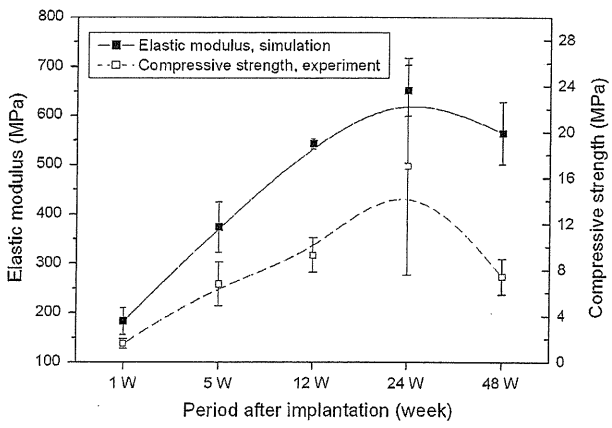

Fig. 7 Variation of measured compressive strength and calculated elastic modulus with duration after implantation

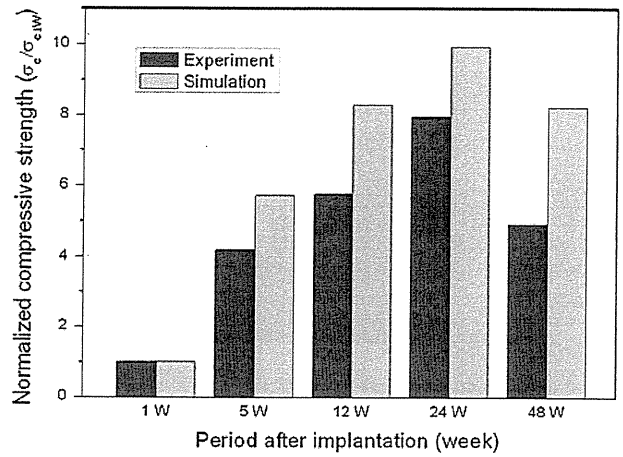

Fig. 8 Normalization of the FE predicted strength and the experimental ones versus time of implantation

model displaying SED on a section is also presented. It is found that the SED distributions change with the duration of implantation. At the beginning, a severe SED concentration can be observed. And over time after operation, the SED concentration decreased gradually and at the time of 48 weeks after implantation, SED distributed quite evenly.

4 Discussion

The results of this study presented the time-dependent variations in mechanical properties of the implanted NEOBONE® (IPHA) after implantation, which revealed the biomechanical interaction between this porous bioactive ceramics and regenerated bone tissue. HA ceramics have been considered as bone bioactive materials which bond to surrounding osseous tissue and enhance bone tissue formation [24]. The structural configuration of HA including the dimension and morphology of the pores has been shown to be critical in allowing osteoconduction and bone growth into the scaffolds [25]. Another important factor is the interconnected pores for the penetration of bone cells. SEM analysis shows that NEOBONE® (IPHA) has rather spherical pores which are interconnected with each other by window-like openings (Fig. 3), resulting in a large surface area which leads to a high tendency to bioresorb and then induces high bioactivity. In addition, the interconnected pores permit tissue ingrowth and thus anchor the prosthesis with the surrounding bone tissue, leading to good mechanical fixation of implants [26].

In the early stage following surgery of being placed in an osseous defect, porous implants should induce a process similar to bone fracture healing, where the implant porosity is initially invaded by mesenchymal cells, fibroblasts and osteoblasts [27]. In animal experiments with IPHA,

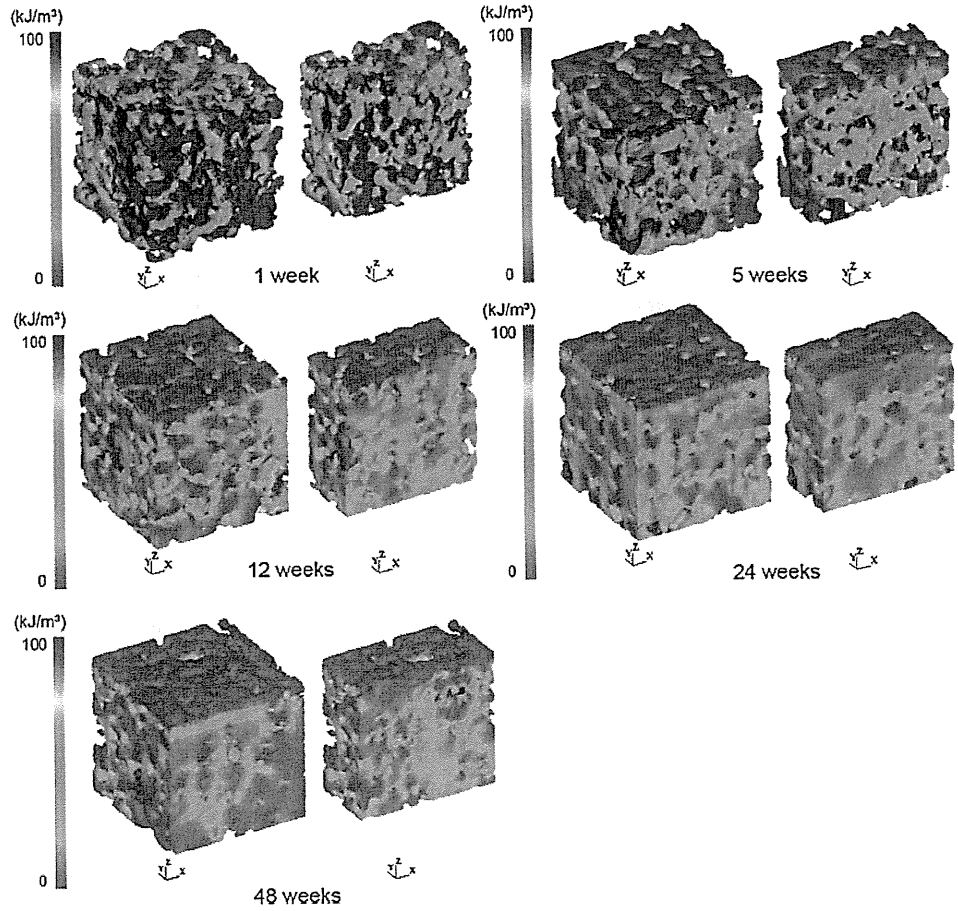

Fig. 9 Distribution of SED of NEOBONE® at 1, 5, 12, 24, and 48 weeks after implantation

interfacial new bone formation was observed at 2 weeks postoperatively and there was a subsequent gradual increase of new bone penetrating into the central area after 5 weeks [1, 9]. The bone formation induces the changes in mineralization. It is known that the altered BMD in turn results in an increase or decrease in the elastic modulus of the bone tissue [28, 29]. Therefore, BMD can be used as predictors of bone stiffness. BMD analysis by dual-energy X-ray absorptiometry [9] demonstrated good correlations with present FE calculated elastic modulus (Fig. 6). In addition, this study presented a computational method to quantify the spatial distribution of elastic moduli (as given in Sect. 2.4). Regarding the obtained results (Fig. 4), no significant differences among all studied periods were observed, though the macro- and microstructure exhibited changes with the duration of surgery. It is understood that the structural changes are caused by bone tissue ingrowth. In terms of the relatively unchanged distribution of elastic moduli, it can be interpreted by the non-resorbability of NEOBONE® as observed in animal experiment [9]. More significantly, it is of great interest to apply this computational method to the resorbable biomaterials, therefore to investigate the effects of degeneration on the spatial distribution of elastic moduli.

In the light of the correlation between bone ingrowth and the overall stiffness, the simulation results are considered to be reasonable. Furthermore, the FE predicted elastic moduli exhibited similar variation with the measured results from compression test (Fig. 5). However, it is noted that the simulation values are a little higher than the experiments except that at 24 weeks (Fig. 5). The higher modulus values obtained from FE models are considered to be caused mostly by the CT resolution. Those pores in the specimens that are smaller than the resolution cannot be recognized in the models. As a result, the FE models have much lower porosities than the corresponding actual specimens. Given that pore connectivity is maintained, HA with larger pore sizes will be weaker as a result of an associated reduction in density. Therefore, the stiffness of the analytical model might be predicted to be higher than that of the actual material. Moreover, the contained soft tissues might have a negative influence on the quality of CT images [16]. This could be one of the reasons for the higher modulus values from FE models. As to the

discrepancy at 24 weeks between experiment and simulation, it can be seen that the experimental value is much higher than the FE predicted one. The causes of this unexpected result are not clear yet and further study is needed to clarify this point.

It is well evidenced that mechanical properties of porous HA are strongly correlated to bone ingrowth. Specifically, experimental observations indicated that compressive strength increased as new bone formed [30–33]. For example, Hing et al. [30] reported that the compressive strength of porous HA derived from cancellous bone increased from 2 to 20 MPa after 3 months in vivo. Trécant et al. [31] reported an increase in the compressive strength of blocks of porous HA/tri-calcium phosphate composites from 3 to 6 MPa after only 1 week in vivo. These results suggest that bone ingrowth have a strong reinforcing effect on porous HA implants. In the current study, the measured compressive strength demonstrated the same trend. Furthermore, it was noted that FE calculated elastic modulus also exhibited similar variation with measured compressive strength, and both parameters reached the highest level at 24 weeks (Fig. 7). The practical significance of the correlation between elastic modulus and strength is that an estimate of elastic modulus (e.g., from FE analysis) may be a predictor for compressive strength. Generally, materials properties do not have such a correspondence, while it exists for bone material, which would suggest a biological linkage between these properties [34, 35]. In the current study, the compressive strength was predicted from the estimated elastic modulus based on the critical strain criterion (as given in Sect. 2.4). The normalized compressive strength versus time of implantation shows well agreements between the simulation and experimental results (Fig. 8). This proposed approach of compressive strength prediction was proved to be feasible in the present application.

Besides the prediction of elastic modulus and compressive strength, FE method enables to get an insight into other mechanical variables, such as stress, strain, and SED. Actually, as a physical scalar related to both stress and strain, the SED has been widely applied as a criterion for bone adaptation and tissue differentiation algorithms [15, 36, 37]. At the microscopic scale, bone growth at the scaffold surface is considered to be regulated by the local SED. In the case of current study, a severe SED concentration existed in the early postoperative period and SED became to distribute evenly at 48 weeks after the implantation (Fig. 9). This result suggested that a process similar to normal remodeling occurred within NEOBONE®. The SED is assumed to be a mechanobiological signal or stimulus that bone cells detect [37, 38], though the fundamental nature is unknown, regarding how the bone cells sense and adapt to the stimuli. However, the existence of strain energy sensors has not been documented in experiments. In this sense, computational models could provide insight into the mechanical factors that affect bone ingrowth, and thereby contribute to better understanding of mechanobiological mechanisms.

The CT-based three-dimensional FE analysis has demonstrated its advantages in evaluating the time-dependent biomechanical changes in porous bioceramics. In spite of the limitation of CT resolution, the validity and efficiency of FE analysis in assessing the influence of bone ingrowth on the mechanical behavior of porous bioceramics have been confirmed. In clinical application, the changes of compressive strength and stiffness after implantation are important for surgeons to select appropriate materials for different surgical applications. Furthermore, the biomechanical behaviors of bone substitute after implantation are critical to assessing the clinical effectiveness and predicting the long-term success of grafts and restorative systems. This study has enabled to investigate the mechanical properties of porous implant after insertion by means of micro-imaging reconstruction and FE method. The CT based FE method may someday demonstrate the feasibility of clinical application that could help assess the mechanical properties of porous implants in individual patient, though there are numerous challenges associated with the biomechanical characterization in vivo. There are methods with better resolution than the micro-CT used here (for example use of a synchrotron [39]). In the future study, we would like to construct more accurate analytical models in accordance with the progress of CT resolution and contribute to a potential quantitative approach for the evaluation of the mechanical properties of such biomaterials.

5 Conclusions

This study enables to evaluate the time-dependent biomechanical changes of porous bioceramics after implantation by a computational approach. Results demonstrated that the variations of mechanical properties are highly correlated to the biomechanical interaction between the porous bioactive ceramics and regenerated bone tissue. Good correspondence between the FE analysis results and the experimental data confirms the feasibility and validity of the future application of this computational approach in the field of bone tissue engineering. With the availability of higher resolution X-ray computed tomography imaging systems for in vivo observation, it would enable researchers to rapidly acquire biomechanical assessment of bone ingrowth after implantation and to predict the long-term success of bone grafts.

Acknowledgments This work was supported in part by The Grant-in-Aid for Highly Functional Interface Science: Innovation of Biomaterials with Highly Functional Interface to Host and Parasite from the Ministry of Education, Science, Sports, and Culture of Japan.

References

1. Tamai N, Myoui A, Tomita T, Nakase T, Tanaka J, Ochi T, Yoshikawa H. Novel hydroxyapatite ceramics with an interconnective porous structure exhibit superior osteoconduction in vivo. J Biomed Mater Res. 2002;59:110–7.
2. Iwai T, Harada Y, Imura K, Iwabuchi S, Murai J, Hiramatsu K, Myoui A, Yoshikawa H, Tsumaki N. Low-intensity pulsed ultrasound increases bone ingrowth into porous hydroxyapatite ceramic. J Bone Miner Metab. 2007;25:392–9.
3. Ng AM, Tan KK, Phang MY, Aziyati O, Tan GH, Isa MR, Aminuddin BS, Naseem M, Fauziah O, Ruszymah BH. Differential osteogenic activity of osteoprogenitor cells on HA and TCP/HA scaffold of tissue engineered bone. J Biomed Mater Res A. 2008;85:301–12.
4. Yoshikawa H, Myoui A. Bone tissue engineering with porous hydroxyapatite ceramics. J Artif Org. 2005;8:131–6.
5. Sopyan I, Mel M, Ramesh S, Khalid KA. Porous hydroxyapatite for artificial bone applications. Sci Technol Adv Mater. 2007;8:116–23.
6. Lu JX, Flautre B, Anselme K, Hardouin P, Gallur A, Descamps M, Thierry B. Role of interconnections in porous bioceramics on bone recolonization in vitro and in vivo. J Mater Sci Mater Med. 1999;10:111–20.
7. Omae H, Mochizuki Y, Yokoya S, Adachi N, Ochi M. Effects of interconnecting porous structure of hydroxyapatite ceramics on interface between grafted tendon and ceramics. J Biomed Mater Res A. 2006;79:329–37.
8. Cyster LA, Grant DM, Howdle SM, Rose FR, Irvine DJ, Freeman D, Scotchford CA, Shakesheff KM. The influence of dispersant concentration on the pore morphology of hydroxyapatite ceramics for bone tissue engineering. Biomaterials. 2005;26:697–702.
9. Yamasaki N, Hirao M, Nanno K, Sugiyasu K, Tamai N, Hashimoto N, Yoshikawa H, Myoui A. A comparative assessment of synthetic ceramic bone substitutes with different composition and microstructure in rabbit femoral condyle model. J Biomed Mater Res B Appl Biomater. 2009;91:788–98.
10. Yoshida Y, Osaka S, Tokuhashi Y. Clinical experience of novel interconnected porous hydroxyapatite ceramics for the revision of tumor prosthesis: a case report. World J Surg Oncol. 2009;7:76.
11. Jaecques SV, Van Oosterwyck H, Muraru L, Van Cleynenbreugel T, De Smet E, Wevers M, Naert I, Vander Sloten J. Individualised, micro CT-based finite element modelling as a tool for biomechanical analysis related to tissue engineering of bone. Biomaterials. 2004;25:1683–96.
12. Lacroix D, Chateau A, Ginebra MP, Planell JA. Micro-finite element models of bone tissue-engineering scaffolds. Biomaterials. 2006;27:5326–34.
13. Sandino C, Planell JA, Lacroix D. A finite element study of mechanical stimuli in scaffolds for bone tissue engineering. J Biomech. 2008;41:1005–14.
14. Byrne DP, Lacroix D, Planell JA, Kelly DJ, Prendergast PJ. Simulation of tissue differentiation in a scaffold as a function of porosity, Young's modulus and dissolution rate: application of mechanobiological models in tissue engineering. Biomaterials. 2007;28:5544–54.
15. Sturm S, Zhou S, Mai YW, Li Q. On stiffness of scaffolds for bone tissue engineering–a numerical study. J Biomech. 2010;43:1738–44.
16. Bessho M, Ohnishi I, Matsuyama J, Matsumoto T, Imai K, Nakamura K. Prediction of strength and strain of the proximal femur by a CT-based finite element method. J Biomech. 2007;40:1745–53.
17. Sepulveda P, Binner JG, Rogero SO, Higa OZ, Bressiani JC. Production of porous hydroxyapatite by the gel-casting of foams and cytotoxic evaluation. J Biomed Mater Res A. 2000;50:27–34.
18. He LH, Standard OC, Huang TT, Latella BA, Swain MV. Mechanical behaviour of porous hydroxyapatite. Acta Biomater. 2008;4:577–86.
19. Keyak JH, Rossi SA, Jones KA, Skinner HB. Prediction of femoral fracture load using automated finite element modeling. J Biomech. 1998;31:125–33.
20. Boccaccini AR, Fan Z. A new approach for the Young's modulus-porosity correlation of ceramic materials. Ceram Int. 1997;23:239–45.
21. Luo J, Stevens R. Porostity-dependence of elastic moduli and hardness of 3Y-TZP ceramics. Ceram Int. 1999;25:281–6.
22. Pabst W, Gregorová E, Tichá G. Elasticity of porous ceramics–a critical study of modulus-porosity relations. J Eur Ceram Soc. 2006;26:1085–97.
23. Gibson LJ. Biomechanics of cellular solids. J Biomech. 2005;38:377–99.
24. Ducheyne P, Qiu Q. Bioactive ceramics: the effect of surface reactivity on bone formation and bone cell function. Biomaterials. 1999;20:2287–303.
25. Gauthier O, Bouler JM, Aguado E, Pilet P, Daculsi G. Macroporous biphasic calcium phosphate ceramics: influence of macropore diameter and macroporosity percentage on bone ingrowth. Biomaterials. 1998;19:133–9.
26. De Aza PN, Luklinska ZB, Santos C, Guitian F, De Aza S. Mechanism of bone-like formation on a bioactive implant in vivo. Biomaterials. 2003;24:1437–45.
27. Hing KA, Best SM, Tanner KE, Bonfield W, Revell PA. Quantification of bone ingrowth within bone-derived porous hydroxyapatite implants of varying density. J Mater Sci Mater Med. 1999;10:663–70.
28. Carter DR, Hayes WC. Bone compressive strength: the influence of density and strain rate. Science. 1976;194:1174–6.
29. Kienapfel H, Sprey C, Wilke A, Griss P. Implant fixation by bone ingrowth. J Arthroplast. 1999;14:355–68.
30. Hing KA, Best SM, Tanner KE, Bonfield W, Revell PA. Biomechanical assessment of bone ingrowth in porous hydroxyapatite. J Mater Sci Mater Med. 1997;8:731–6.
31. Trécant M, Delécrin J, Royer J, Goyenvalle E, Daculsi G. Mechanical changes in macro-porous calcium phosphate ceramics after implantation in bone. Clin Mater. 1994;15:233–40.
32. Martin RB, Chapman MW, Sharkey NA, Zissimos SL, Bay B, Shors EC. Bone ingrowth and mechanical properties of coralline hydroxyapatite 1 yr after implantation. Biomaterials. 1993;14:341–8.
33. Hernandez CJ, Beaupré GS, Keller TS, Carter DR. The influence of bone volume fraction and ash fraction on bone strength and modulus. Bone. 2001;29:74–8.
34. Fyhrie DP, Vashishth D. Bone stiffness predicts strength similarly for human vertebral cancellous bone in compression and for cortical bone in tension. Bone. 2000;26:169–73.
35. Liu X, Niebur GL. Bone ingrowth into a porous coated implant predicted by a mechano-regulatory tissue differentiation algorithm. Biomech Model Mechanobiol. 2008;7:335–44.
36. Sanz-Herrera JA, García-Aznar JM, Doblaré M. On scaffold designing for bone regeneration: a computational multiscale approach. Acta Biomater. 2009;5:219–29.
37. Ruimerman R, Van Rietbergen B, Hilbers P, Huiskes R. The effects of trabecular-bone loading variables on the surface

signaling potential for bone remodeling and adaptation. Ann Biomed Eng. 2005;33:71–8.
38. Huiskes R, Ruimerman R, van Lenthe GH, Janssen JD. Effects of mechanical forces on maintenance and adaptation of form in trabecular bone. Nature. 2000;405:704–6.
39. Nogueira LP, Braz D, Barroso RC, Oliveira LF, Pinheiro CJ, Dreossi D, Tromba G. 3D histomorphometric quantification of trabecular bones by computed microtomography using synchrotron radiation. Micron. 2010;41:990–6.

Biochemical and Biophysical Research Communications 416 (2011) 205–210

Contents lists available at SciVerse ScienceDirect

Biochemical and Biophysical Research Communications

journal homepage: www.elsevier.com/locate/ybbrc

Nkx3.2-induced suppression of Runx2 is a crucial mediator of hypoxia-dependent maintenance of chondrocyte phenotypes

Yoshitaka Kawato [a], Makoto Hirao [b], Kosuke Ebina [a], Noriyuki Tamai [a], Kenrin Shi [a], Jun Hashimoto [b], Hideki Yoshikawa [a], Akira Myoui [c,*]

[a] Department of Orthopaedics, Graduate School of Medicine, Osaka University, 2-2 Yamadaoka, Suita, Osaka 565-0871, Japan
[b] Department of Orthopaedic Surgery, National Hospital Organization, Osaka Minami Medical Center, 2-1 Kidohigashi, Kawachinagano, Osaka 586-8521, Japan
[c] Medical Center for Translational Research, Osaka University Hospital, 2-15 Yamadaoka, Suita, Osaka 565-0871, Japan

ARTICLE INFO

Article history:
Received 28 October 2011
Available online 10 November 2011

Keywords:
Hypoxia
Nkx3.2
Transcription factor
Endochondral ossification

ABSTRACT

Hypoxia is a key factor in the maintenance of chondrocyte identity. However, crucial chondrogenic transcription factors in the Sox families are not activated in this phenomenon, indicating that other pathways are involved.

Nkx3.2 is a well-known chondrogenic transcription factor induced by Sonic hedgehog (Shh); it suppresses a key osteogenic transcriptional factor, Runt-related transcription factor 2 (Runx2), to maintain the chondrogenic phenotype in mesenchymal lineages. The purpose of this study was to examine the function of Nkx3.2 in hypoxia-dependent maintenance of chondrocyte identity.

C3H10T1/2 pluripotent mesenchymal cells were cultured with rh-BMP2 (300 ng/ml) to induce chondrogenesis under normoxic (20% O_2) or hypoxic (5% O_2) conditions.

Immunohistological detection of Nkx3.2 in a micromass cell culture system revealed that hypoxia promoted expression of the Nkx3.2 protein. Real-time RT-PCR analysis revealed that hypoxia promoted *Nkx3.2* mRNA expression and suppressed *Runx2* mRNA expression; however, *Sox9* mRNA expression was not altered by oxygen conditions, as previously described. Over-expression of exogenous Nkx3.2 promoted glycosaminoglycan (GAG) production and inhibited *Runx2* mRNA expression and, based on a dual luciferase assay, *Runx2* promoter activity. Interestingly, downregulation of *Nkx3.2* using RNAi abolished hypoxia-dependent GAG production and restored *Runx2* mRNA expression and promoter activity.

These results demonstrated that Nkx3.2-dependent suppression of Runx2 was a crucial factor in hypoxia-dependent maintenance of chondrocyte identity.

1. Introduction

A number of pathophysiological findings indicate that a correlation exists between hypoxia and chondrogenesis. Articular cartilage is an avascular tissue to which nutrients and oxygen are supplied by diffusion from synovial fluid and subchondral bone. Articular chondrocytes may normally persist in 1–6% O_2 [1–4], which is very hypoxic relative to the atmosphere. Additionally, hypoxia-inducible factor 1 (Hif-1), one of the major mediators of the hypoxic response, is essential for chondrocyte growth arrest and survival [5]. Therefore, hypoxia is considered to be a key factor in chondrogenesis. Recently, we found that hypoxia (5% O_2) promotes chondrogenic differentiation and that hypoxia is necessary for maintenance of chondrocyte identity [6]. Interestingly, this phenomenon did not involve the upregulation of *Sox9*, a key chondrogenic transcription factor [6]. However, the details of the mechanisms by which hypoxia maintains chondrocyte identity remain unclear. To further investigate these mechanisms, we focused on Nkx3.2, a transcription factor that represses Runx2 [7].

During endochondral ossification, chondrocytes undergo hypertrophy and secrete an extracellular matrix, which becomes mineralized and allows vascular invasion to initiate osteoblastic differentiation [8]. Runx2 is essential for inducing chondrocyte hypertrophy [9–12] and osteoblastic differentiation [13–15]. Under hypoxic conditions, downregulation of Runx2 activity inhibits osteoblastic differentiation and/or hypertrophy of chondrocytes [6].

The transcription factor Nkx3.2 (also called Bapx1), the vertebrate homolog of *Drosophila* bagpipe, is initially induced by Sonic Hedgehog (Shh) signaling in paraxial mesoderm, and Nkx3.2 promotes the commitment of mesenchymal cells to chondrocyte

Abbreviations: Shh, Sonic hedgehog; Runx2, Runt related transcription factor 2; BMP, bone morphogenic protein; GAG, glycosaminoglycan; RNAi, RNA interference; siRNA, small interference RNA; Hif-1, hypoxia-inducible factor 1; SMMD, spondylomegaepiphysial-metaphysial dysplasia; Col2a1, type II collagen α1; PTHrP, parathyroid hormone-related protein; Ihh, Indian hedgehog; ALP, alkaline phosphatase.

* Corresponding author. Fax: +81 6 6879 6549.
E-mail address: myoi@hp-mctr.med.osaka-u.ac.jp (A. Myoui).

0006-291X/$ - see front matter © 2011 Elsevier Inc. All rights reserved.
doi:10.1016/j.bbrc.2011.11.026

differentiation [16–18]. Nkx3.2 represses Runx2 gene expression and a Runx2 transcriptional reporter [7].

Based on these observations, we speculated Nkx3.2 may play an important role in hypoxia-dependent maintenance of chondrocyte phenotype by suppressing Runx2.

Here, we investigated role of Nkx3.2 in the mechanism by hypoxia maintains chondrocyte phenotypes.

2. Materials and methods

2.1. Cell culture

C3H10T1/2 cells were obtained from RIKEN Bio-Resource Center (Saitama, Japan) and were cultured in Dulbecco's modified Eagle's medium (Invitrogen, San Diego, CA). The cells were incubated at 37 °C under 5% CO_2 and 20% O_2 (normoxia) or 5% O_2 (hypoxia) with or without recombinant human BMP-2 (300 ng/ml). BMP-2 stimulation was when cell monolayers reached 90% confluence.

2.2. High-density micromass cell culture and immunocytochemistry

Cells were spot-seeded; 50 μl drops containing 5×10^5 cells were placed in individual chambers of a Lab-Tek Chamber Slide System (Thermo Fisher Scientific Inc., Waltham, MA) [19]. After cells attached to the substrate (approximately 2 h), they were stimulated with rh-BMP2 (300 ng/ml) and cultured under normoxic or hypoxic conditions. After 72 h, cells were fixed in 10% formalin for anti-Nkx3.2 antibody staining.

2.3. Assessment of chondrocyte differentiation

To evaluate chondrogenic differentiation, C3H10T1/2 cells were fixed with 10% formalin, washed with 0.1 N HCl in distilled water; cells were then stained with alcian blue solution, alcian blue 8GX (Sigma, St. Louis, MO). To quantify chondrogenic differentiation, the absorbance of alcian blue dye bound to sulfated glycosaminoglycan (GAG) was measured [20]. All experiments were performed in triplicate.

2.4. Antibodies and reagents

Recombinant human BMP-2 was provided by Osteopharma Inc., Osaka, Japan. Anti-mouse Nkx3.2 antibodies were purchased from Santa Cruz Biotechnology, Inc., Santa Cruz, CA.

2.5. DNA constructs

An expression plasmid encoding wild-type Nkx3.2 (WT-Nkx3.2) was constructed by inserting a full-length *Nkx3.2* cDNA into the pBApo-CMV Neo vector purchased from Takara Bio Inc., Otsu, Japan.

2.6. Reporter constructs and luciferase reporter assay

A tandem array of six Runx2 binding site were inserted into the pGL3-Promoter vector (Promega, Madison, WI), and the recombinant plasmid was designated 6Runx2E-Luc. A tandem array of eight Nkx3.2 binding site were inserted into the pGL3-Promoter vector (Promega), and this construct was designated 8Nkx3.2E-Luc. Reporter assays were performed by transient transfection of 0.4 μg of the pGL3-Promoter vectors (8Nkx3.2E-Luc or 6Runx2E-Luc) and 0.01 μg of the TK-*Renilla* luciferase construct (TK *Renilla*) (Promega). Luciferase activity was measured using a Dual Luciferase assay kit (Promega) and luminometer (Berthold Technologies, Bad Wildbad, Germany); luciferase activity was normalized to *Renilla* luciferase activity, an internal standard. All experiments were performed in triplicate.

Table 1
Sequences of siRNA duplex targeting *Nkx3.2* mRNA and of siRNA control.

Target gene	Oligonucleotide	Sequence (5′ → 3′)
Negative control	Sense	ATCCGCGCGATAGTACGTA
Nkx3.2	Sense	CCAAGGACCUGGAGGAGGATT

Table 2
Sequences of PCR primers used to amplify each gene in standard and quantitative RT-PCR.

Gene	Primer	Sequence (5′ → 3′)
Col2a1	Forward	CCTGTCTGCTTCTTGTAAAAC
	Reverse	AAAAAATACAGAGGTGTTTGACACAGA
Nkx3.2	Forward	AGATGTCAGCCAGCGTTTC
	Reverse	AGGGCTAACGCTGTCATCCT
Sox9	Forward	ATGAATCTCCTGGACCCCTT
	Reverse	AACTTTGCCAGCTTGCACGT
Runx2	Forward	GCTTGATGACTCTAAACCTA
	Reverse	AAAAAGGGCCCAGTTCTGAA
Shh	Forward	TTAACCATCAGCGCTACCTG
	Reverse	CCTTTACGGCCACTTTCTTG
PTHrP	Forward	ATGACAAGGGCAAGTCCATC
	Reverse	CGTCTCCACCTTGTTGGTTT
Ihh	Forward	TCAGTGATGTGCTTATTTTC
	Reverse	CCTTGTGAGAGGAGCATAGG
GAPDH	Forward	TGAACGGGAAGCTCACTGG
	Reverse	TCCACCACCCTGTTGCTGTA

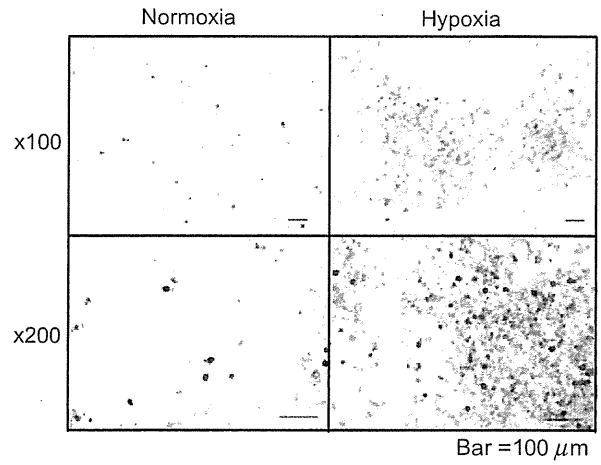

Fig. 1. Hypoxia upregulated Nkx3.2 protein. Immunostaining for Nkx3.2 protein. C3H10T1/2 cells were seeded at high density (1×10^5 cells/10 μl) on chamber slides. They were stimulated with BMP-2 (300 ng/ml) and cultured under normoxic or hypoxic conditions for 72 h. The cell cultures were then fixed and immunostained using anti-Nkx3.2 antibody. Nkx3.2 protein expression was higher under hypoxic than under normoxic conditions. Original magnification of upper panel is 100×, lower panel is 200×. Bar = 100 μm.

2.7. RNA interference of Nkx3.2

RNA interference was done using commercially synthesized siRNA (B-Bridge International, Inc., Cupertino, CA) and the protocols provided by the manufacturer. Cells were transfected with 10 μM Lipofectamine RNAiMAX (Invitrogen). The sequences of

siRNA duplex targeting Nkx3.2 mRNA and of negative control siRNA are shown in Table 1.

2.8. Standard and quantitative RT-PCR

First-strand cDNA was synthesized using SuperScript III RNase H® reverse transcriptase (Invitrogen). Standard RT-PCR was performed using Ex Taq (Takara Bio Inc.). Quantitative RT-PCR was performed using the Roche Applied Science Light Cycler system. The SYBR Green assay, in which each cDNA sample was evaluated in triplicate 20 μl reactions, was used for all target transcripts. Expression values were normalized to *GAPDH*. The sequence of specific primers used for standard and quantitative RT-PCR assays, are shown in Table 2.

2.9. Statistical analysis

All data are expressed as means ± standard deviation (SD) of a minimum of three replicate measurements. Differences between groups were assessed using the Student's *t*-test. Any p value <0.05 was considered statistically significant.

3. Results

3.1. Nkx3.2 protein was upregulated under hypoxia

To investigate whether oxygen tension changed the expression of Nkx3.2 protein, we measured protein expression using an immunocytochemistry assay and a micromass cell culture system.

In C3H10T1/2 cell condensation culture, expression of Nkx3.2 protein was higher under hypoxia than normoxia (Fig. 1).

3.2. Hypoxia upregulated Nkx3.2 mRNA and a Nkx3.2 reporter construct

To investigate the function of Nkx3.2 in hypoxia-dependent maintenance of chondrocyte identity, we performed a real-time RT-PCR analysis and a dual luciferase activity assay. Expression

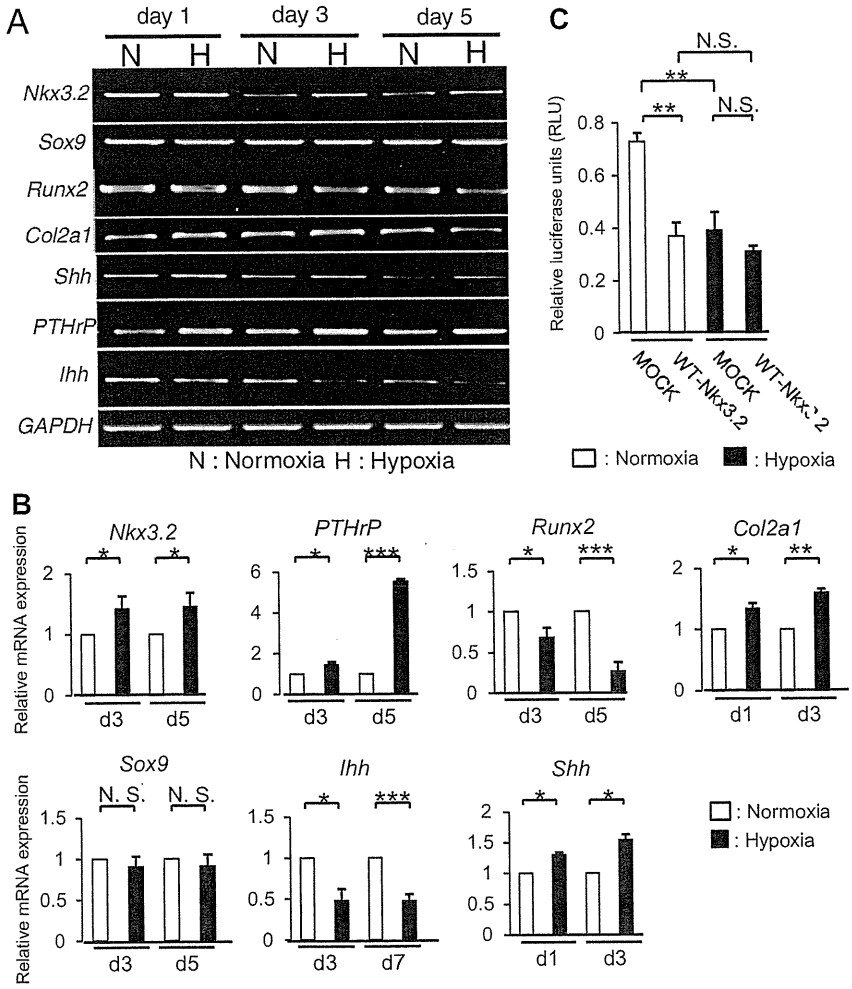

Fig. 2. Hypoxia upregulated *Nkx3.2* mRNA expression and a *Nkx3.2* reporter construct. (A) On days 1, 3, and 5, total RNA was extracted from C3H10T1/2 cells that were cultured with BMP-2 (300 ng/ml) and under normoxic or hypoxic conditions. RT-PCR was performed to generate *Nkx3.2*, *Sox9*, *Runx2*, *Col2a1*, *Shh*, *PTHrP*, *Ihh*, and *GAPDH* cDNA. (B) Real-time RT-PCR assays of *Nkx3.2*, *Sox9*, *Runx2*, *Col2a1*, *Shh*, *PTHrP*, *Ihh*, and *GAPDH* expression were performed. Expression values were normalized to the level of *GAPDH* mRNA. Data shown for each measurement are the mean ± SD of three replicate samples. $^{*}P < 0.05$; $^{**}P < 0.01$; $^{***}P < 0.001$. (C) C3H10T1/2 cells were co-transfected with 8Nkx3.2E-Luc and TK-*Renilla* reporter constructs. After transfection (12 h), cells were incubated with BMP-2 (300 ng/ml) and cultured under normoxic or hypoxic condition for 3 days. Luciferase activity was measured and normalized by determining *Renilla* luciferase activity. Data shown for each measurement are the mean ± SD of three replicate samples. $^{**}P < 0.01$; *N.S.*, not significant.

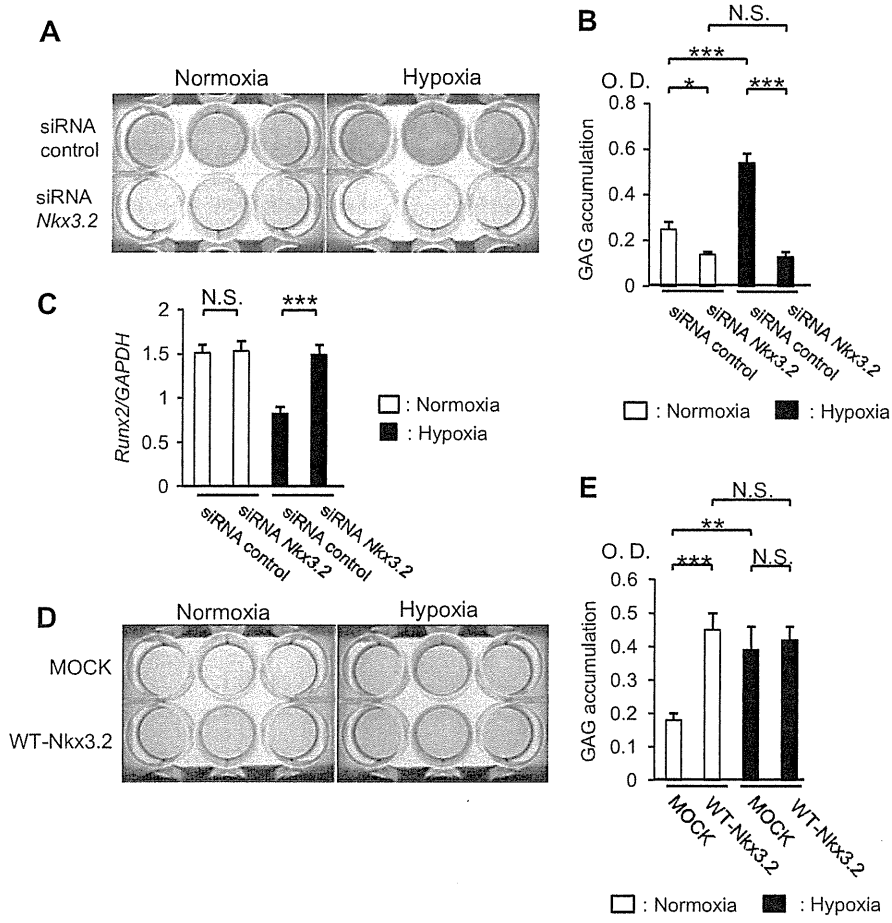

Fig. 3. Nkx3.2 was a positive regulator of hypoxia-dependent GAG production. (A–C) Forty-eight hours after transfection with siRNA control (upper wells) or with *Nkx3.2* siRNA (lower wells), C3H10T1/2 cells were stimulated with BMP-2 (300 ng/ml) and cultured under normoxic or hypoxic condition for 5 days. (A,D) Cells were stained with alcian blue. (B,E) Quantification of GAG synthesis in C3H10T1/2 cells on day 5. Data shown for each measurement are the mean ± SD of three replicate samples. ***$P < 0.001$; *N.S.*, not significant. (C) Total RNA was extracted and real time RT-PCR for *Runx2* was performed. Values were normalized to the level of *GAPDH* mRNA. Data for each measurement are the mean ± SD of three replicate samples. ***$P < 0.001$; *N.S.*, not significant. (D) Twenty-four hours after transfection with MOCK (upper wells) or with WT-Nkx3.2 (lower wells), C3H10T1/2 cells were stimulated with BMP-2 (300 ng/ml) and cultured under normoxic or hypoxic condition for 5 days. Cells were then stained with alcian blue.

of *Nkx3.2*, *Col2a1*, *Shh*, and *PTHrP* mRNAs was higher in hypoxic conditions than in normoxic conditions. In contrast, *Runx2* and *Ihh* were downregulated in hypoxic conditions, while *Sox9* was not affected by the differences in oxygen tension (Fig. 2A and B). As Nkx3.2 usually suppresses transcription, upregulation of *Nkx3.2* transcriptional activity may result in downregulation of the 8Nkx3.2E-Luc reporter construct. In normoxia, WT-Nkx3.2 reduced 8Nkx3.2E-Luc activity. In hypoxia, basal suppressive transcription of *Nkx3.2* was upregulated, and WT-Nkx3.2 did not affect 8Nkx3.2E-Luc activity (Fig. 2C).

3.3. Nkx3.2 was a positive regulator of hypoxia-dependent GAG production

Inhibition of endogenous *Nkx3.2* using RNAi abolished GAG production in C3H10T1/2 cell cultures, especially in those cultures under hypoxia. In addition, knockdown of *Nkx3.2* completely restored the hypoxia-dependent downregulation of *Runx2* mRNA (Fig. 3A–C). Conversely, Nkx3.2 overexpression using WT-Nkx3.2 promoted GAG production in normoxic C3H10T1/2 cultures; GAG production in these cultures was similar to that in hypoxic cultures. Notably, Nkx3.2 overexpression did not affect GAG production in hypoxic cultures (Fig. 3D and E).

3.4. Over-expression of Nkx3.2 using WT-Nkx3.2 downregulated Runx2 mRNA and a Runx2 reporter construct

WT-Nkx3.2 downregulated *Runx2* mRNA in hypoxic and especially in normoxic cultures (Fig. 4A and B). Additionally, WT-Nkx3.2 downregulated the *Runx2* reporter to similar extent in hypoxic and normoxic cultures (Fig. 4C).

4. Discussion

Murine mesenchymal C3H10T1/2 cells are pluripotent and can differentiate into chondrocytes following BMP-2 or BMP-7 treatment [21–23]. Moreover, BMP-2 treatment and low oxygen tension synergistically induce GAG production and *Col2a1* mRNA expression and substantially suppress ALP activity and mineralization [6]. These findings indicate that hypoxia promotes chondrogenic differentiation and inhibits osteoblastic differentiation of pluripotent C3H10T1/2 mesenchymal cells.

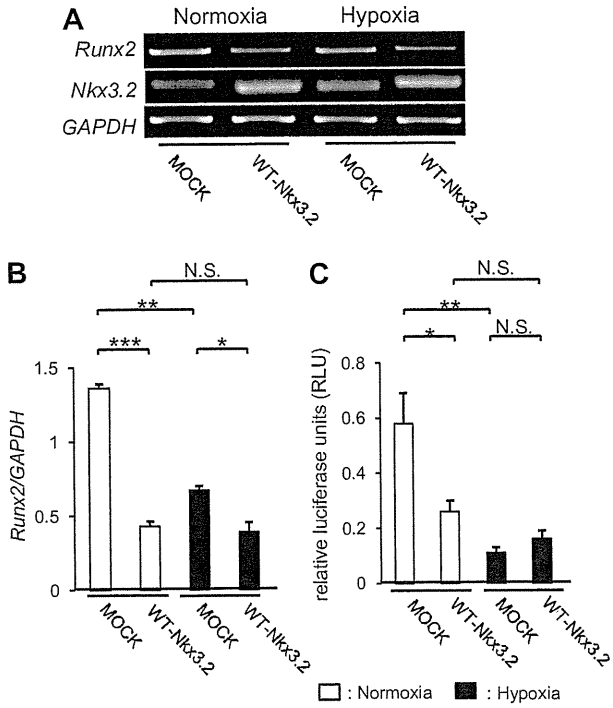

Fig. 4. Nkx3.2 downregulated *Runx2* mRNA expression and activity *Runx2* reporter construct. (A) After transfection (24 h) with MOCK or with WT-Nkx3.2, C3H10T1/2 cells were stimulated with BMP-2 (300 ng/ml) and cultured under normoxic or hypoxic condition for 5 days. Total RNA was extracted and RT-PCR was used to measure *Runx2*, *Nkx3.2*, and *GAPDH* mRNA expression. (B) Real time RT-PCR for *Runx2*, *Nkx3.2*, and *GAPDH* were performed. Values are normalized to the level of *GAPDH* mRNA. Data are for each measurement are the mean ± SD of three replicate samples. $^{*}P < 0.05$; $^{**}P < 0.01$; $^{***}P < 0.001$. (C) C3H10T1/2 cells were co-transfected with 6Runx2E-Luc and TK-*Renilla* reporter constructs. After transfection (12 h), cells were incubated with BMP-2 (300 ng/ml) and cultured under normoxic or hypoxic condition for 3 days. Luciferase activity was measured and normalized by determining *Renilla* luciferase activity. Data for each measurement are the mean ± SD of three replicate samples. $^{*}P < 0.05$; $^{**}P < 0.01$; *N.S.*, not significant.

Hif-1 is a major mediator of the response to hypoxia, but knockdown of Hif-1 using an adenoviral virus vector system did not abolish hypoxia-induced GAG production in our preliminary experiments (data not shown), suggesting no significant relationship between hypoxia-induced chondrogenesis and Hif-1.

Here, we confirmed that hypoxia upregulated *Nkx3.2* mRNA expression, a *Nkx3.2* reporter construct (Fig. 2A–C), and expression of endogenous Nkx3.2 protein in C3H10T1/2 cell micromass cell culture (Fig. 1). Furthermore, *Runx2* mRNA expression and a *Runx2* reporter construct were significantly downregulated by both hypoxia and overexpression of exogenous wild-type Nkx3.2 (Fig. 4). Because siRNAs complementary to *Nkx3.2* mRNA abolished hypoxia-dependent GAG production and *Runx2* downregulation, it is plausible that hypoxia-dependent upregulation of Nkx3.2 is essential for hypoxia-dependent GAG production and Runx2 suppression. These data indicated that Nkx3.2 was a crucial transcription factors that suppressed Runx2 and, consequently, mediated hypoxia-induced chondrogenic differentiation and the subsequent hypoxia-dependent maintenance of chondrocyte identity.

Previous findings indicate that Shh signaling induces expression of two sclerotomal genes *Nkx3.2* and *Sox9*, which are both known to promote cartilage formation [16–18]. Conversely, PTHrP signals block chondrocyte hypertrophy by both Nkx3.2-dependent and -independent pathways [24,25]. Here, hypoxia upregulated *Shh* and *PTHrP* mRNA expression (Fig. 2A and B), but it was unclear why hypoxia-induced upregulation of *Shh* did not alter *Sox9* mRNA expression. Additionally, although hypoxia-induced upregulation of PTHrP may be involved in Nkx3.2-independent Runx2 downregulation, our findings from the *Nkx3.2* knockdown experiment indicated that Nkx3.2 may have primarily contributed to hypoxia-dependent Runx2 suppression via Shh and PTHrP upregulation. From these observations, it is reasonable to propose that hypoxia-induced Nkx3.2 upregulation via Shh, together with hypoxia-induced PTHrP contributed to the inhibition of chondrocyte hypertrophy by suppressing Runx2 expression.

As shown in Fig. 3, over-expression of Nkx3.2 and inhibition of *Nkx3.2* clearly affected GAG production in C3H10T1/2 cell, indicating that Nkx3.2 may have affected chondrogenic differentiation.

However, this study had several limitations. We used only one cell line in this experiment. In addition, future studies should confirm which factors function upstream of Nkx3.2 in hypoxia-induced chondrogenesis and the mechanisms by which Nkx3.2 promotes chondrogenic differentiation.

In conclusion, we demonstrated that Nkx3.2 was crucial for hypoxia-dependent maintenance of chondrocyte identity.

Role of the funding source

This work was supported by grants from the Japan Science and Technology Agency.

Disclosure statement

All authors have no conflicts of interest.

Acknowledgment

The authors thank Mrs. Mari Shinkawa for her technical assistance.

References

[1] K.H. Falchuk, E.J. Goetzl, J.P. Kulka, Respiratory gases of synovial fluids. An approach to synovial tissue circulatory-metabolic imbalance in rheumatoid arthritis, Am. J. Med. 49 (1970) 223–231.
[2] P.S. Treuhaft, D.J. McCarty, Synovial fluid pH, lactate, oxygen and carbon dioxide partial pressure in various joint diseases, Arthritis Rheum. 14 (1971) 475–484.
[3] T. Kiaer, J. Gronlund, K.H. Sorensen, Subchondral pO_2, pCO_2, pressure, pH, and lactate in human osteoarthritis of the hip, Clin. Orthop. Relat. Res. 229 (1988) 149–155.
[4] W.R. Ferrell, H. Najafipour, Changes in synovial PO_2 and blood flow in the rabbit knee joint due to stimulation of the posterior articular nerve, J. Physiol. 449 (1992) 607–617.
[5] E. Schipani, H.E. Ryan, S. Didrickson, T. Kobayashi, M. Knight, R.S. Johnson, Hypoxia in cartilage: HIF-1alpha is essential for chondrocyte growth arrest and survival, Genes Dev. 15 (2001) 2865–2876.
[6] M. Hirao, N. Tamai, N. Tsumaki, H. Yoshikawa, A. Myoui, Oxygen tension regulates chondrocyte differentiation and function during endochondral ossification, J. Biol. Chem. 281 (2006) 31079–31092.
[7] C.J. Lengner, M.Q. Hassan, R.W. Serra, C. Lepper, A.J. van Wijnen, J.L. Stein, J.B. Lian, G.S. Stein, Nkx3.2-mediated repression of Runx2 promotes chondrogenic differentiation, J. Biol. Chem. 280 (2005) 15872–15879.
[8] H.M. Kronenberg, Developmental regulation of the growth plate, Nature 423 (2003) 332–336.
[9] M. Inada, T. Yasui, S. Nomura, S. Miyake, K. Deguchi, M. Himeno, M. Sato, H. Yamagiwa, T. Kimura, N. Yasui, T. Ochi, N. Endo, Y. Kitamura, T. Kishimoto, T. Komori, Maturational disturbance of chondrocytes in Cbfa1-deficient mice, Dev. Dyn. 214 (1999) 279–290.
[10] S. Takeda, J.P. Bonnamy, M.J. Owen, P. Ducy, G. Karsenty, Continuous expression of Cbfa1 in nonhypertrophic chondrocytes uncovers its ability to induce hypertrophic chondrocyte differentiation and partially rescues Cbfa1-deficient mice, Genes Dev. 15 (2001) 467–481.
[11] C.A. Yoshida, H. Yamamoto, T. Fujita, T. Furuichi, K. Ito, K. Inoue, K. Yamana, A. Zanma, K. Takada, Y. Ito, T. Komori, Runx2 and Runx3 are essential for chondrocyte maturation, and Runx2 regulates limb growth through induction of Indian hedgehog, Genes Dev. 18 (2004) 952–963.
[12] I.S. Kim, F. Otto, B. Zabel, S. Mundlos, Regulation of chondrocyte differentiation by Cbfa1, Mech. Dev. 80 (1999) 159–170.

[13] F. Otto, A.P. Thornell, T. Crompton, A. Denzel, K.C. Gilmour, I.R. Rosewell, G.W. Stamp, R.S. Beddington, S. Mundlos, B.R. Olsen, P.B. Selby, M.J. Owen, Cbfa1, a candidate gene for cleidocranial dysplasia syndrome, is essential for osteoblast differentiation and bone development, Cell 89 (1997) 765–771.
[14] S. Mundlos, F. Otto, C. Mundlos, J.B. Mulliken, A.S. Aylsworth, S. Albright, D. Lindhout, W.G. Cole, W. Henn, J.H. Knoll, M.J. Owen, R. Mertelsmann, B.U. Zabel, B.R. Olsen, Mutations involving the transcription factor CBFA1 cause cleidocranial dysplasia, Cell 89 (1997) 773–779.
[15] T. Komori, H. Yagi, S. Nomura, A. Yamaguchi, K. Sasaki, K. Deguchi, Y. Shimizu, R.T. Bronson, Y.H. Gao, M. Inada, M. Sato, R. Okamoto, Y. Kitamura, S. Yoshiki, T. Kishimoto, Targeted disruption of Cbfa1 results in a complete lack of bone formation owing to maturational arrest of osteoblasts, Cell 89 (1997) 755–764.
[16] L.C. Murtaugh, L. Zeng, J.H. Chyung, A.B. Lassar, The chick transcriptional repressor Nkx3.2 acts downstream of Shh to promote BMP-dependent axial chondrogenesis, Dev. Cell 1 (2001) 411–422.
[17] L. Zeng, H. Kempf, L.C. Murtaugh, M.E. Sato, A.B. Lassar, Shh establishes an Nkx3.2/Sox9 autoregulatory loop that is maintained by BMP signals to induce somitic chondrogenesis, Genes Dev. 16 (2002) 1990–2005.
[18] D.M. Cairns, M.E. Sato, P.G. Lee, A.B. Lassar, L. Zeng, A gradient of Shh establishes mutually repressing somitic cell fates induced by Nkx3.2 and Pax3, Dev. Biol. 323 (2008) 152–165.
[19] M.R. Seghatoleslami, R.S. Tuan, Cell density dependent regulation of AP-1 activity is important for chondrogenic differentiation of C3H10T1/2 mesenchymal cells, J. Cell. Biochem. 84 (2002) 237–248.
[20] Y.B. Lim, S.S. Kang, T.K. Park, Y.S. Lee, J.S. Chun, J.K. Sonn, Disruption of actin cytoskeleton induces chondrogenesis of mesenchymal cells by activating protein kinase C-alpha signaling, Biochem. Biophys. Res. Commun. 273 (2000) 609–613.
[21] T. Katagiri, A. Yamaguchi, T. Ikeda, S. Yoshiki, J.M. Wozney, V. Rosen, E.A. Wang, H. Tanaka, S. Omura, T. Suda, The non-osteogenic mouse pluripotent cell line, C3H10T1/2, is induced to differentiate into osteoblastic cells by recombinant human bone morphogenetic protein-2, Biochem. Biophys. Res. Commun. 172 (1990) 295–299.
[22] I. Asahina, T.K. Sampath, P.V. Hauschka, Human osteogenic protein-1 induces chondroblastic, osteoblastic, and/or adipocytic differentiation of clonal murine target cells, Exp. Cell Res. 222 (1996) 38–47.
[23] E.A. Wang, D.I. Israel, S. Kelly, D.P. Luxenberg, Bone morphogenetic protein-2 causes commitment and differentiation in C3H10T1/2 and 3T3 cells, Growth Factors 9 (1993) 57–71.
[24] S. Provot, H. Kempf, L.C. Murtaugh, U.I. Chung, D.W. Kim, J. Chyung, H.M. Kronenberg, A.B. Lassar, Nkx3.2/Bapx1 acts as a negative regulator of chondrocyte maturation, Development 133 (2006) 651–662.
[25] J. Fischer, A. Dickhut, M. Rickert, W. Richter, Human articular chondrocytes secrete parathyroid hormone-related protein and inhibit hypertrophy of mesenchymal stem cells in coculture during chondrogenesis, Arthritis Rheum. 62 (2010) 2696–2706.

OPEN ACCESS Freely available online

PLoS one

P38 Mitogen-Activated Protein Kinase Inhibitor, FR167653, Inhibits Parathyroid Hormone Related Protein-Induced Osteoclastogenesis and Bone Resorption

Huiren Tao[1,2☯], Mina Okamoto[1☯], Masataka Nishikawa[1], Hideki Yoshikawa[1], Akira Myoui[1]*

1 Department of Orthopedics, Osaka University Graduate School of Medicine, Osaka, Japan, **2** Department of Orthopedics, Xijing Hospital, Fourth Military Medical University, Xi'an, China

Abstract

p38 mitogen-activated protein kinase (MAPK) acts downstream in the signaling pathway that includes receptor activator of NF-κB (RANK), a powerful inducer of osteoclast formation and activation. We investigated the role of p38 MAPK in parathyroid hormone related protein (PTHrP)-induced osteoclastogenesis *in vitro* and PTHrP-induced bone resorption *in vivo*. The ability of FR167653 to inhibit osteoclast formation was evaluated by counting the number of tartrate-resistant acid phosphatase positive multinucleated cells (TRAP-positive MNCs) in *in vitro* osteoclastgenesis assays. Its mechanisms were evaluated by detecting the expression level of c-Fos and nuclear factor of activated T cells c1 (NFATc1) in bone marrow macrophages(BMMs) stimulated with sRANKL and M-CSF, and by detecting the expression level of osteoprotegerin (OPG) and RANKL in bone marrow stromal cells stimulated with PTHrP in the presence of FR167653. The function of FR167653 on bone resorption was assessed by measuring the bone resorption area radiographically and by counting osteoclast number per unit bone tissue area in calvaria in a mouse model of bone resorption by injecting PTHrP subcutaneously onto calvaria. Whole blood ionized calcium levels were also recorded. FR167653 inhibited PTHrP-induced osteoclast formation and PTHrP-induced c-Fos and NFATc1 expression in bone marrow macrophages, but not the expression levels of RANKL and OPG in primary bone marrow stromal cells treated by PTHrP. Furthermore, bone resorption area and osteoclast number in vivo were significantly decreased by the treatment of FR167653. Systemic hypercalcemia was also partially inhibited. Inhibition of p38 MAPK by FR167653 blocks PTHrP-induced osteoclastogenesis *in vitro* and PTHrP-induced bone resorption *in vivo*, suggesting that the p38 MAPK signaling pathway plays a fundamental role in PTHrP-induced osteoclastic bone resorption.

Citation: Tao H, Okamoto M, Nishikawa M, Yoshikawa H, Myoui A (2011) P38 Mitogen-Activated Protein Kinase Inhibitor, FR167653, Inhibits Parathyroid Hormone Related Protein-Induced Osteoclastogenesis and Bone Resorption. PLoS ONE 6(8): e23199. doi:10.1371/journal.pone.0023199

Editor: Harish Pant, National Institutes of Health, United States of America

Received June 7, 2011; **Accepted** July 8, 2011; **Published** August 23, 2011

Funding: This work was supported by grants from the Ministry of Education, Culture, Sports, Science and Technology, Japan and by the Ministry of Health, Labor and Welfare, Japan. The funders had no role in study design, data collection and analysis, decision to publish, or preparation of the manuscript.

Competing Interests: The authors have declared that no competing interests exist.

* E-mail: myoi@hp-mctr.med.osaka-u.ac.jp

☯ These authors contributed equally to this work.

Introduction

Parathyroid hormone related protein (PTHrP), a potent stimulator of osteoclastic bone resorption, was first identified as a causative factor for humoral hypercalcemia of malignancy [1]. A number of clinicopathological and experimental studies have shown that cancer cell-derived PTHrP promotes osteoclastic bone resorption and contributes to the development and progression of cancer metastasis to bone [2–5]. PTHrP stimulates osteoclastogenesis by acting on osteoblasts and/or bone marrow stromal cells to increase receptor activator of NF-κB ligand (RANKL) expression and reduce osteoprotegerin (OPG) expression, not by acting directly on osteoclast precursors [6]. Osteoclast precursors that express RANK, a tumor necrosis factor (TNF) receptor family member, recognize RANKL and differentiate into osteoclasts in the presence of macrophage/monocyte colony stimulating factor (M-CSF). OPG is a soluble decoy receptor for RANKL and has the ability to inhibit osteoclastogenesis. Therefore, a relative increase of RANKL versus OPG expression by PTHrP activates osteoclastic bone resorption [7–12].

Additionally, a body of evidence suggested that p38 mitogen-activated protein kinase (MAPK) is downstream of the RANK signaling pathway and plays an important role in osteoclast differentiation. The expression of dominant-negative forms of p38 MAPK in RAW264.7 cells inhibited RANKL-induced differentiation of these cells into osteoclasts [13]. Li et al used pyridinylimidazole SB203580, a specific inhibitor of p38 MAPK, to study p38 MAPK function and demonstrated that p38 MAPK is required for osteoclast differentiation [14].

FR167653 was first discovered as a potent inhibitor of TNFα and interleukin (IL)-1β production in lipopolysaccharide-stimulated human monocytes and phytohemagglutinin-M-stimulated human lymphocytes [15,16]. FR167653 inhibits the activation of p38 MAPK by suppressing the phosphorylation of p38 MAPK, preferentially affecting its α isoform, but not the γ isoform [17–19]. FR167653 is effective in treating inflammation, relieving trauma

and ischemia-reperfusion injury *in vivo* [20–22]. We previously reported that M-CSF-dependent sRANKL- and TNFα-induced osteoclast formation in primary bone marrow cells, and collagen-induced arthritis in rats were inhibited by FR167653 [23]. However, the relationship of p38 MAPK and PTHrP in osteoclastogenesis and bone resorption is still unclear.

Here we investigate the role of FR167653 on PTHrP-induced osteoclastogenesis, local bone resorption, and hypercalcemia. We found that FR167653 not only blocked osteoclast differentiation induced both by PTHrP and sRANKL with down regulation of c-Fos and NFATc1 in bone marrow macrophages without affecting RANKL and OPG expression in bone marrow stromal cells, but also alleviated bone resorption induced by PTHrP with partial reduction of hypercalcemia in vivo.

Materials and Methods

Animal and reagents

All animal experiments in this study strictly followed a protocol approved by the Institutional Animal Care and Use Committee of Osaka University (approval number: 338). Six-week-old male ddy mice and four- to eight-week-old male BDF1 mice were purchased from Japan SLC (Hamamatsu, Japan) and Oriental Yeast (Tokyo, Japan), respectively. Human recombinant PTHrP (1–34) was purchased from Peptide Institute (Osaka, Japan). M-CSF and soluble recombinant RANKL were purchased from PeproTeck EC (London, UK). FR167653 was provided by Asteras Pharma (Osaka, Japan). c-Fos and actin antibodies were purchased from Cell Signaling Technology (Danvers, USA). NFATc1 antibody was bought from BD Biosciences Pharmingen (Franklin Lakes, USA).

Primary bone marrow cell culture

Bone marrow cells were collected by removing the tibias and femurs from ddy mice and flushing the bone cavity with serum-free alpha-minimum essential medium (αMEM; Invitrogen, Carlsbad, CA). A sample of 7.5×10^5 cells in a volume of 0.5 ml/well were cultured in αMEM supplemented with 10% fetal bovine serum (FBS; Equitech-Bio, Kerrville, TX) in the presence of PTHrP (45 ng/ml). Some cultures received an additional treatment of 10 μM, 1 μM or 0.1 μM FR167653. The medium was changed every two days, replacing half of the medium with 0.25 ml fresh medium containing 90 ng/ml PTHrP and 20 μM, 2 μM and 0.2 μM FR167653. After six days of culture, adherent cells were stained for tartrate-resistant acid phosphatase (TRAP), an osteoclast marker enzyme, using a TRAP staining kit (Hokudo, Sapporo, Japan). TRAP-positive multinucleated cells (MNCs) with three or more nuclei were counted as osteoclasts.

M-CSF-dependent bone marrow macrophage (MDBMMs) culture

M-CSF-dependent bone marrow macrophages (MDBMMs) were cultured as described previously [23–25]. Briefly, bone marrow cells (5×10^6) were cultured in the αMEM supplemented with 10% FBS, and M-CSF at the concentration of 100 ng/ml in 100 mm dishes for three days. Then the cells were washed and harvested with 0.02% ethylene diamine tetra-acetate (EDTA) in phosphate-buffered saline, and seeded at a density of 3×10^5 into 100-mm culture dishes in the presence of M-CSF (100 ng/ml). After three more days of culture, the adherent cells were considered as MDBMMs.

For osteoclast culture, MDBMMs were digested with 0.25% Trypsin-EDTA (Invitrogen) and 1×10^4/well cells were re-plated into 48-well plates in the presence of sRANKL (100 ng/ml) and M-CSF (100 ng/ml). Some cultures were treated with FR167653. After five more days of culture, adherent cells were fixed and stained for TRAP. TRAP-positive MNCs containing three or more nuclei were counted as osteoclasts.

For the detection of the c-Fos and NFATc1expression, MDBMMs were treated by each concentration of FR167653 for 1 hour. Then, sRANKL and M-CSF were added. After another 24 or 48 hour culture, the cells were collected for RNA extraction and protein extraction.

Real-time polymerase chain reaction

Total RNA was extracted from bone marrow cells (for genes of OPG and RANKL) or bone marrow macrophages (for genes of c-fos and NFATc1) by using the RNeasy Mini Kit (Qiagen, Valencia, CA). RNase-free DNase Set (Qiagen) was used to remove the residual DNA. Five micrograms of RNA were reverse transcribed into cDNA with Ready-To-Go You-Prime First-Strand Beads (Amersham Bioscience, Piscataway, NJ). In order to reduce pipetting error, the final volume of cDNA was reached by adding four volumes RNase-free distilled water to the original cDNA. The resultant product was subjected to real-time PCR.

Real-time PCR was performed in a Light Cycler (Roche Applied Science, Indianapolis, IN) with Light cycler-DNA Master SYBR Green I (Roche Applied Science) and were performed according to the standard protocol recommended by the manufacturer. Reverse transcription was followed by 40 cycles of PCR (denaturation at 95°C for 10 min addition of 1-second at 94°C, 5-second annealing at 58, 60, 61, 59 and 58°C for OPG, RANKL, c-fos, NFATc1 and GAPDH, respecticvely, and 10-second extension at 72°C, and each of optimal fluorescence measurement temperature for 1 second as the amplification and quantification programs, 60–99°C with a heating rate of 0.1°C per second as the melting curve program, and finally, cooling to 40°C.

The primer sequences are as follows:

RANKL: sense: 5′-CAC CAT CAG CTG AAG ATA GT-3′

antisense: 5′-CCA AGA TCT CTA ACA TGA CG-3′

OPG: sense: 5′-TGGGACCAAAGTGAATGCC-GAGA-3′

antisense: 5′-AGCTGCTCTGTGGTGAGGTTC-3′

c-fos: sense: 5′-CTGGTGCAGCCCACTCTGGT-3′

antisense: 5′- CTTTCAGCAGATTGGCAATC-3′

NFATc1: sense: 5′- CAACGCCCTGACCACCGATA-3′

antisense: 5′- GGCTGCCTTCCGTCTCATAG-3′

GAPDH: sense: 5′-ACCACAGTCCATGCCATCAC-3′

antisense: 5′- TCCACCACCCTGTTGCTGTA-3′

Semiquantitative RANKL, OPG, c-fos and NFATc1 expression levels were determined by normalizing with GAPDH expression level.

Western blotting

Cells were washed twice with ice-cold PBS and lysed with a buffer containing 20 mM Tris–HCl, 150 mM NaCl, 1% riton X-100, and inhibitors for proteases and phosphatases [25]. Cell lysates were centrifuged at 10,000 g for 20 min and the supernatants were collected. Twenty micrograms of cellular

proteins was resolved by SDS-PAGE and transferred onto nitrocellulose membranes. Membranes were blocked with 5% skim milk in Tris-buffered saline containing 0.1% Tween 20 for 1 h and incubated overnight at 4°C with primary antibodies. Membranes were washed, incubated with appropriate secondary antibodies conjugated to horseradish peroxidase for 1 h, and developed using a chemiluminescence system. Relative protein expression was calculated from band densities obtained in three experiments using UMax PowerLook 1100 scanner (Taiwan) and TotalLab gel image analysis software (Nonlinear Dynamics, New England, UK).

PTHrP-induced bone resorption in an animal model

Male BDF1 mice aged four weeks were injected daily for five days (from day one to five) with PTHrP (18 μg/day; Figure 1). PTHrP was injected into the subcutaneous tissue over the left side of the calvaria twice daily in a volume of 10 μl as described previously [26,27]. This delivery method produces an exaggerated resorptive response in the calvarial bone, as well as a systemic effect as indicated by hypercalcemia. Animals were housed in an accredited facility and all procedures used in the animal experiments complied with the standards described in the Osaka University Medical School Guidelines for the Care and Use of Laboratory Animal.

Treatment Protocol

All animals were additionally treated with FR167653 or distilled water, injected subcutaneously on the mice back as in the protocol shown in Figure 1. Treatment was initiated two days before PTHrP injection.

Before treatment, 50 μl of whole blood was collected retro-orbitally into heparinized capillary tubes (Radiometer, Copenhagen, Denmark) and basal whole-blood ionized calcium levels were determined with a calcium level analyzer (model ABL505, Radiometer; n = 3 from treatment group and control group, respectively). The treatment group (n = 7) was treated with 30 mg/kg of FR167653 twice daily while the control group (n = 5) was treated with distilled water for seven days (including pretreatment). At day three and five, blood samples were taken three hours after injection of PTHrP retro-orbitally to determine the levels of hypercalcemia. Mice were killed on day six, which was 12 hours after the last injection of PTHrP.

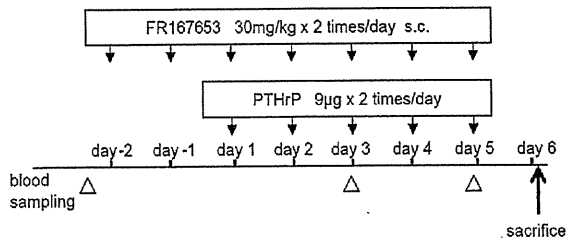

Figure 1. Animal model and treatment protocol. The PTHrP-induced bone resorption animal model was established by injecting PTHrP (18 μg/day) onto the dorsal surface of the mice calvaria daily for five days (day 1 to 5). Animals in the treatment (n = 7) or the control group (n = 5) were injected with FR167653 (30 mg/kg twice daily) or distilled water, respectively, daily for seven days, initiating from two days before PTHrP injection. 50 μl of whole blood was collected retro-orbitally before treatment, on day three, and on day five to determine whole-blood ionized calcium levels. Mice were sacrificed on day six, 12 hours after the last injection of PTHrP.
doi:10.1371/journal.pone.0023199.g001

Quantitative analysis of bone resorption

Calvaria were retrieved from sacrificed mice and immersed into neutral buffered formalin. Radiographs were taken with the MX-20 Specimen Radiography System (Faxitron X-ray, Wheeling, IL). The images were scanned into a computer with a flatbed scanner and saved in RGB color format. The quantitative analysis of calvarial bone resorption was processed with an image analysis software package, WinROOF (Mitani, Fukui, Japan). The thresholds were determined by clicking five typical bone resorptive areas.

After decalcification, the anterior and posterior portions of the calvaria were removed just anterior to coronal suture and posterior to lambdoid suture, respectively. The left part of the calvaria was cut into three strips, embedded in paraffin and sectioned. Sections were stained to detect TRAP activity and counterstained with hematoxylin.

Histomorphometic analysis was performed on the left side of the calvaria to determine the number of osteoclasts present in the bone. The area measured consisted of six visual fields extending from sagittal suture toward the lateral muscle attachment and included all of the bone and marrow spaces. PTHrP-treated calvaria showed a distinct dorsal periosteal pattern of resorption and endosteal resorption. Thus, the osteoclast number represented the sum of periosteal and endosteal measurements. Results were recorded as osteoclast number per unit bone tissue area measured (OcN-BTA). All measurements were made by tracing the section image onto a digitizing platen with the aid of a cameral lucida attachment and WinROOF image analysis software.

Statistical analysis

All analyses were reported as mean ±S.D. Statistical significance was evaluated by Student's *t*-test or one factor analysis of variance (ANOVA) followed by a Tukey-Kramer post test using a statistical software package, JMP (SAS institute, Cary, NC).

Results

FR167653 inhibits Osteoclast formation in two different cell culture systems

To determine whether FR167653 blocks osteoclastogenesis *in vitro*, we investigated osteoclastogenesis in a primary bone marrow cells stimulated by PTHrP. As expected, TRAP-positive MNCs (osteoclasts) was formed in primary bone marrow cultures treated with PTHrP. As shown in Figure 2, osteoclast formation induced by PTHrP at day six was inhibited by addition of FR167653 in a dose-dependent manner. At the concentration of 10 μM, FR167653 nearly eliminated osteoclast formation.

Unlike bone marrow cells, MDBMM cells are a homogeneous bone marrow macrophage population with a contamination by stromal cells of less than 1 in 1,000 cells. As shown in Figure 3, MDBMM cells formed TRAP-positive osteoclasts when treated with RANKL together with M-CSF even in the absence of stromal cells. FR167653 added to the cultures significantly inhibited RANKL-induced osteoclast formation in a dose-dependent manner. These data suggest that FR167653 acts directly on osteoclast precursors to inhibit osteoclast formation.

OPG and RANKL expression levels in bone marrow cells were not affected by FR167653 treatment

To further elucidate the mechanism of FR167653 inhibition of PTHrP-induced osteoclastogenesis, we examined the effects of FR167653 on the OPG and RANKL expression in bone marrow stromal cells.